21th Annual CFD Symposium,
August 8-9, 2019, Bangalore

ANSYS SCALE RESOLVING SIMULATIONS OF LAUNCH-VEHICLE CONFIGURATION AT TRANSONIC SPEEDS

Krishna Zore[1]
(krishna.zore@ansys.com)
ANSYS, Inc.
Plot no. 34/1, Hinjewadi, Pune-411057,
Maharashtra, India

Balasubramanyam Sasanapuri[2]
(balasubramanyam.sasanapuri@ansys.com)
ANSYS, Inc.
Unit no. 906, The Platina, Gachibowli, Hyderabad-500032, Telangana, India

Mohammad Azab[3]
(mohammad.azab@ansys.com)
ANSYS, Inc.
10 Cavendish Ct, Lebanon, NH 03766, USA

Shoaib Shah[4], **John Stokes**[5]
(shoaib.shah@ansys.com,
John.stokes@ansys.com)
ANSYS, Inc.
1000 Sherbrooke Street West, Suite 2120,
Montreal QC, H3A 3G4 Canada

ABSTRACT

The pressure fluctuations that cause aero-acoustic noise at transonic speed are predicted using a high-fidelity scale resolving turbulence model. The Stress-Blended Eddy Simulation *(SBES)*, a hybrid RANS-LES model, in ANSYS Fluent is used on the NASA Technical Memorandum X-646[1] 'Fineness-ratio-2' test configuration, defined as an ellipsoidal nose on a cylindrical body with a 30^0 backward facing step *(model-IV)*. Results computed for two different conditions are compared against the experimental measurements[1]. While RANS models show good agreement with experimental measurements for steady pressure coefficient *(C_P)* predictions, notably observed for a variety of transonic speeds and angles of attack with ANSYS Fluent Shear Stress Transport k-ω *(SST)* turbulent model, accurate predictions of the unsteady pressure fluctuations and power spectral densities *(PSD)* at shock and step-wake regions require suitable numerical discretization schemes as well as temporal and spatial resolution of larger turbulent fluctuations. The accuracy of PSD calculations is critical for obtaining good predictions of buffet loading in the design of launch vehicle structures. This paper outlines these requirements in more detail and proposes appropriate mesh and numerics settings in order to capture the flow physics with the desired level of solution accuracy.

Key words: Buffeting, SBES, Aerodynamics, Turbulent, CFD, SRS

NOMENCLATURE

k = Turbulent kinetic energy.
ω = Dissipation rate.
SST = Shear Stress Transport.
M = Mach number.
α = Angle of attack.
LES = Large Eddy Simulation
SRS = Scale Resolved Simulation.
SBES = Stress-Blended Eddy Simulation.
RANS = Reynolds-Averaged Navier-Stokes.
ρ = Density.
μ = Molecular viscosity.
T = Temperature.
P = Pressure.
γ = Gas constant.
PSD = Power Spectral Density
C_p = Pressure coefficient,
ΔC_p (RMS) = Coefficient of the root-mean-square fluctuations of pressure about the mean
Re = Reynolds number
D = Maximum body diameter
f = frequency
CAD = Computer-aided design
RMS = Root mean square
BOI – Body of Influence

INTRODUCTION

Launch vehicles exiting the earth's atmosphere traverse through transonic range and can encounter large structural loads because of the large pressure gradients in the presence of shock waves[2]. Furthermore, the shock waves are inherently unsteady and can trigger pressure fluctuations which are amplified by step-wake separation and can cause flow instabilities called buffeting[1-8], which impose a structural design problem due to local panel loading, over-all structural excitation and/or transmitting unsteady loads on delicate payloads or guidance instruments[1,2,3]. The significance of such pressure fluctuations and power spectral densities on various launch vehicle shapes *(bodies of revolution)* within transonic speed range have been extensively studied by Charles[1] at NASA Ames 14-foot transonic wind tunnel. These studies drew five conclusions: 1. The pressure fluctuations and possible unsteady bending on vehicles with a cylindrical body with an ellipsoidal nose of fineness ratio 2 or a conical nose of 14-1/2^0 half-cone angle is small; 2. reducing the cross-sectional area behind the slender nose results in flow separation, which in turn causes pressure fluctuations over the entire vehicle area; 3. The sharpness with which the vehicle area is reduced in the converging section affects the Mach number range and hence the unsteady pressures; 4. the maximum pressure fluctuations on a vehicle with inter-stage flares having cylindrical sections with different diameters but equal preceding cone angle is approximately the same; 5. PSDs are not particular to any specific vehicle profile but depends on the location within the flow.

In this paper, ANSYS Fluent R19.2 is used to predict transonic flows with unsteady shock waves and step-wake generated pressure fluctuations on the 'Fineness-ratio-2' test configuration, referred to as ellipsoidal nose on cylindrical body with 30^0 backward facing step *(model-IV).*

The unstructured meshes used for the simulations are prepared using ANSYS Fluent Meshing R19.2. Several mesh-refinement levels (from coarse to fine) for a single test condition are first studied, comparing only the steady-state pressure coefficient *(C_p)* distributions with experimental measurements. Based on these initial steady-state solutions, the meshes are then further optimized in order to capture the mean and unsteady root-mean-square (RMS) pressure fluctuations with ANSYS Fluent SBES model.

Finally, these results are then compared against the experimental measurements for the test conditions defined in Table 2.

GEOMETRY AND MESH

The launch-vehicle *(model-IV)* geometric dimensions are taken from the NASA Technical Memorandum X-646[1]. Figure 1a shows the 2D sketch with the model dimensions. These dimensions are used to prepare a model geometry using ANSYS Discovery SpaceClaim R19.2 3D CAD modelling tool. Figure 1b shows the model-IV CAD geometry that was created.

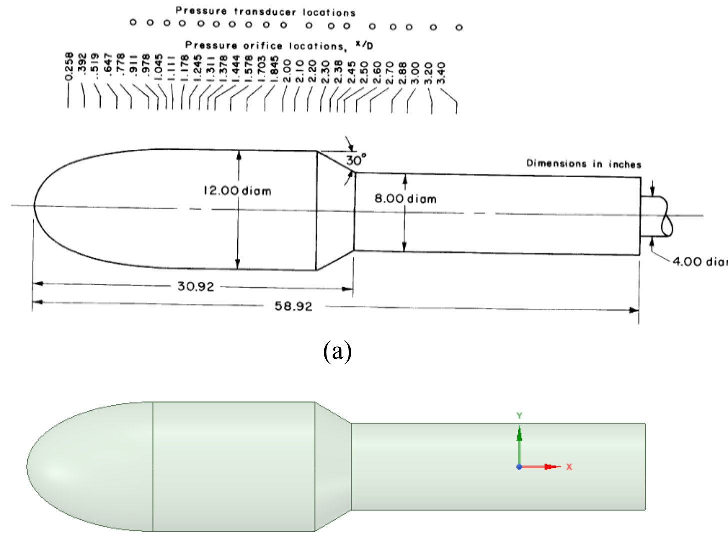

Figure 1. Fineness-ratio-2 ellipsoidal nose on cylindrical body with 30^0 backward facing step (model-IV), (a) Schematic sketch dimensions[1], (b) CAD model.

Table 1. Computational mesh details.

Mesh labels	Mesh levels	Mesh type	No. of volume elements (million)
Mesh 1	Coarse	Hexcore	1.3
Mesh 2	Medium	Hexcore	4.2
Mesh 3	Fine	Hexcore	27
Mesh-Opt1	Optimize	Hexcore	55
Mesh-Opt2		Mosaic Poly-Hexcore	34

The unstructured Hexcore meshes are prepared using ANSYS Fluent Meshing R19.2. Table 1. provides information on the mesh refinement levels and the numbers of volume elements. Three refinement levels of Hexcore mesh *(coarse, medium and fine)* are prepared and the results are compared against the experimental measurements to select a baseline mesh for completing the test matrix runs. Figure 2 and Figure 3 show the surface and volume mesh refinements corresponding to the mesh refinements levels: (a) coarse, (b) medium, and (c) fine.

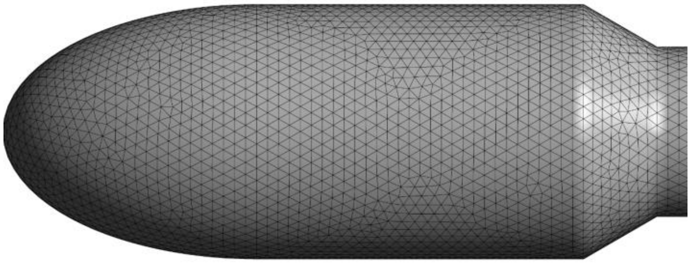

(a)

(b)

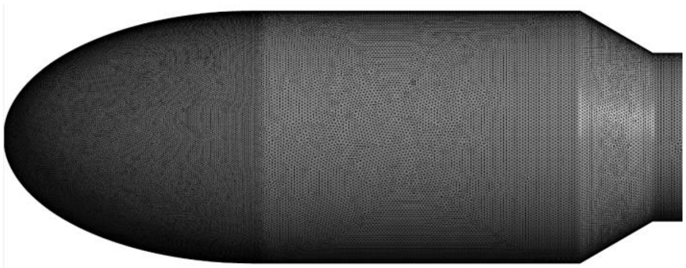

(c)

Figure 2. Model-IV, surface mesh refinement, Hexcore, (a) Coarse, (b) Medium, and (c) Fine.

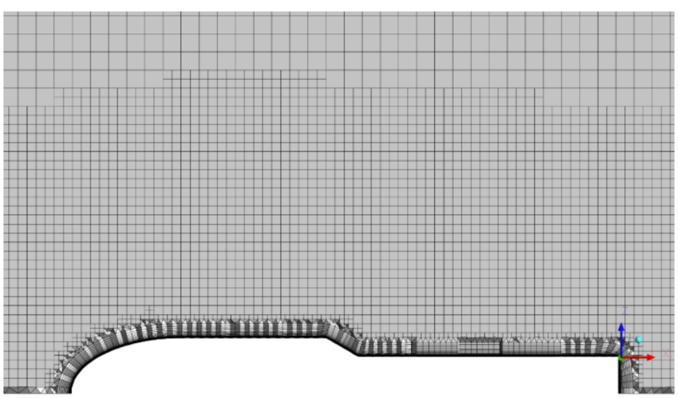

(a)

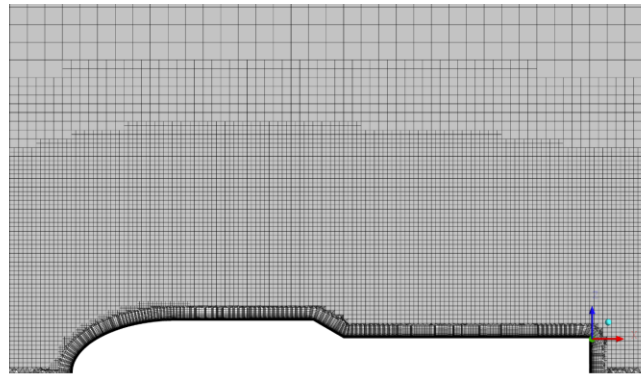

(b)

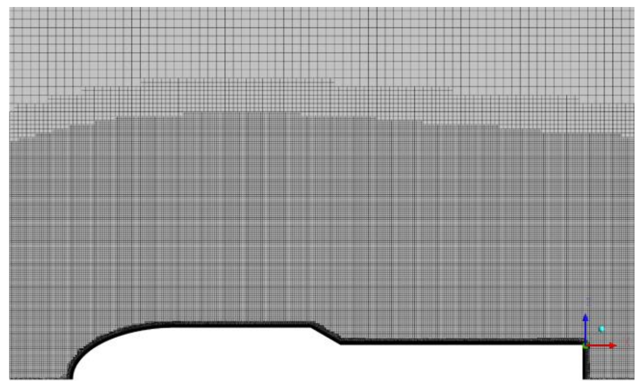

(c)

Figure 3. Model-IV, volume mesh refinement, Hexcore, (a) Coarse, (b) Medium, and (c) Fine.

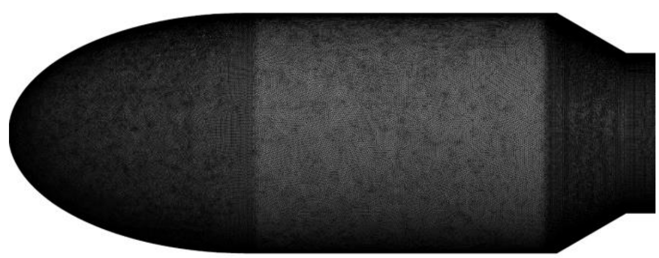

(a)

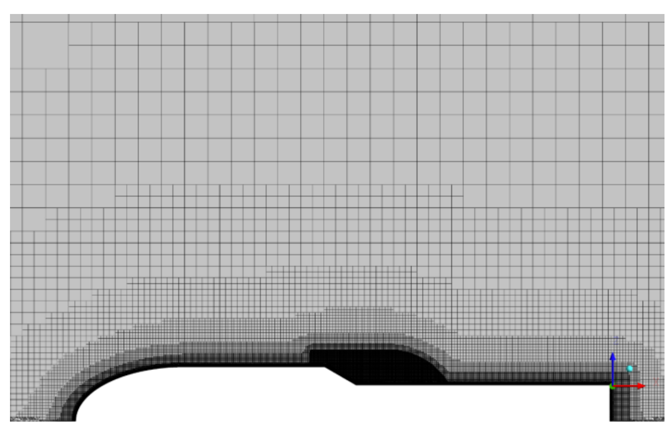

(b)

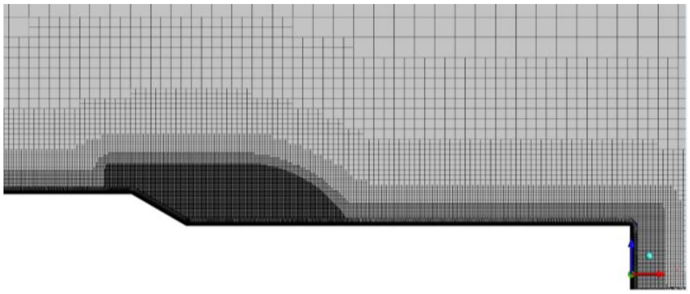

(c)

Figure 4. Mesh-Opt1, (a) surface mesh, (b) & (c) Volume refinement.

A further optimized Hexcore mesh (Mesh-Opt1) is prepared based on the need to resolve the transient turbulent structures in the step wake flow region accurately. Figure 4 shows this optimized Hexcore mesh: (4a) the surface mesh, (4b) the volume refinement around the model-VI, and (4c) the volume refinement in the step wake. Additionally, an optimized Poly-Hexcore mesh (Mesh-Opt2) is prepared using ANSYS Fluent Meshing Mosaic^{TM} technology[13]. The Poly-Hexcore feature in ANSYS Fluent uses this technology to fill the bulk region with high-quality octree hexahedrals, layered polyprism mesh in the boundary layer, and conformally connect the two meshes with general polyhedral elements. This results in a reduction of approximately 40% in the total element count compared to the conventional Hexcore mesh, as seen in Table 1., correspondingly leading to a substantial ANSYS Fluent solver speed up, in some applications by as much as 50%. Figure 5a and Figure 5b show the surface and volume mesh resolution of the conventional Hexcore and the Mosaic Poly-Hexcore mesh, respectively. Numerous validations of this Mosaic technology in predicting complex aerodynamic forces on the Automotive and Aerospace industrial applications can be found in Ref. 14 & 15.

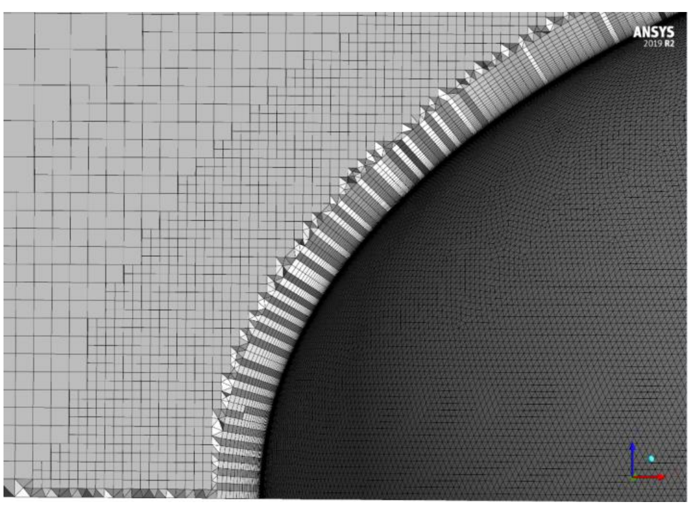

(a)

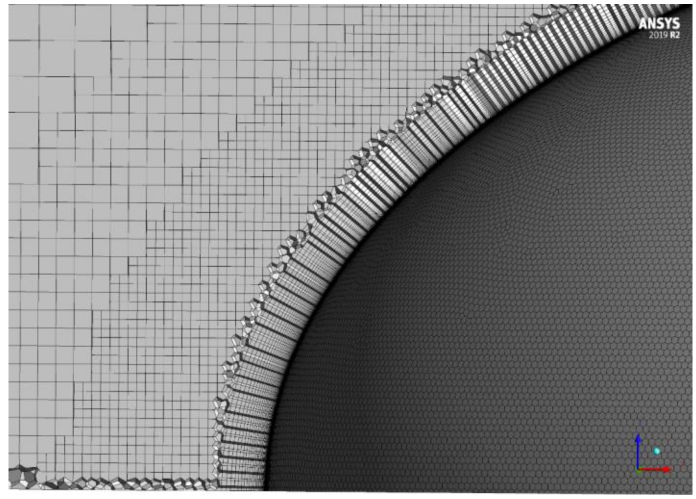

(b)

Figure 5. (a) Mesh-Opt1 (Hexcore), (b) Mesh-Opt2 (Mosaic Poly-Hexcore).

TEST CONDITIONS

The test conditions for this validation study are illustrated in Table 2. One angle of attack and two Mach numbers are simulated in the transonic flow regimes. Experimental mean and RMS fluctuating pressure coefficients are available for the conditions presented in this paper.

Table 2. Test Conditions.

Conditions	Angle of attack (deg)	Mach Number
I	0	0.79
II	0	0.925

SOLVER NUMERICS

The CFD simulations are performed using ANSYS Fluent R19.2, which uses a cell-centered finite volume method. The pressure-based solver with coupled pressure-velocity scheme is applied using Green-Gauss node-based spatial discretization method for gradients and 2nd order upwind for pressure and turbulence. The Bounded Central Differencing (BCD) scheme is used for the momentum equation, which enables low numerical diffusion using Central Differencing Scheme, but still ensures stability by blending in First and Second Order Upwind Schemes when and where required. This scheme is based on the normalized variable diagram and only switches to first order when convection boundedness is violated[16]. To further improve gradient accuracy, a Warped-Face Gradient Correction *(WFGC)* method is enabled, which corrects gradient accuracy degradation due to very high aspect ratio cells, non-flat faced cells in the boundary layers, and any highly deformed cells with cell centroid outside of the control volume. A second order implicit iterative dual time-advancement method is used for the transient formulations.

The transient Scale Resolved Simulations *(SRS)* are performed using the hybrid RANS-LES SBES turbulence closure model. The SBES model uses a RANS model for near wall flows and LES for the large detached flows. The main differentiator of the SBES model compared to Detached Eddy Simulations (DES) and Delayed DES *(DDES) models* is a much stronger shielding function f_{SBES} for the RANS region. Also, the SBES model shows faster transition between RANS and LES regions, leading to lower eddy viscosity and more resolved turbulence, and with that making SBES model well-suited for highly separated shear layer flows[9,10]. The turbulence stress tensor blending is illustrated below in Equation 1.

$$\tau_{ij}^{SBES} = \tau_{ij}^{RANS}\, f_{SDES} + \tau_{ij}^{LES}\,(1 - f_{SDES}) \tag{1}$$

where τ_{ij}^{RANS} is the RANS and τ_{ij}^{LES} is the LES part of the modeled stress tensors. The SBES model also provides flexibility to choose different model formulations for the RANS and the LES parts. If the RANS and LES parts are modeled based on eddy-viscosity formulation, which they are in this study, the eddy-viscosity of the SBES model is defined as in Equation 2.

$$V_{ij}^{SBES} = V_{ij}^{RANS}\, f_{SDES} + V_{ij}^{LES}\,(1 - f_{SDES}) \tag{2}$$

Where, V_{ij}^{RANS} is the RANS and V_{ij}^{LES} is the LES sub-grid scale modeled eddy-viscosity. The main purpose of the LES models is to provide enough damping of the smallest *(unresolved)* scales. Thus, it is advisable to use simple algebraic LES models, of which the Smagorinsky[11] *(1963)* model is the most widely used. However, the main deficiency of the Smagorinsky model is that its eddy-viscosity does not go to zero for laminar shear flows. Hence, it is desirable to have simple LES formulation which can automatically provide zero eddy-viscosity for simple laminar shear flows, and this is achieved by Wall-Adapting Local Eddy-viscosity *(WALE)* model developed by Nicoud and Ducros[12] *(1999)*. This is available as default in the ANSYS Fluent solver and is used for this investigation.

RESULTS AND DISCUSSIONS

In this section, the computational results are compared with the experimental measurements for the model-IV launch-vehicle obtained from the NASA Technical Memorandum X-646[1].

Figure 5. shows the steady-state RANS (mean) pressure coefficient *(C_p)* computed for the M = 0.79 and $\alpha = 0^0$ test condition, measured along the top center line of the model and compared against the experimental data. The plot illustrates that the C_p predicted by the Hexcore mesh refinement levels; coarse, medium and fine converging towards the experimental values with each refinement level, especially close to the step-wake region. However, the differences between each refinement level is very small and the overall C_p prediction among the meshes is similar on the front and the middle portions of the model. The C_p plot also indicates that the shock front is located at approximately X/D = 0.8, as indicated by the sharp decrease in the suction peak.

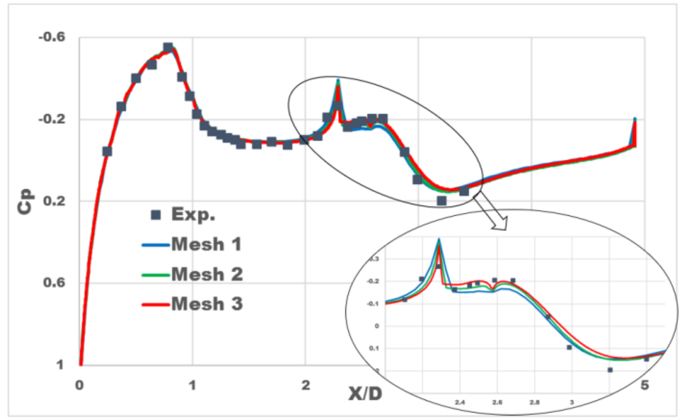

Figure 5. Model-IV, Condition-I, Mesh Study, Steady-State RANS (mean) Pressure Coefficient (C_p) compares with the experimental measurements.

Given the higher accuracy of the Mesh 3 simulations compared to experimental results, Condition-II is thus only calculated with this mesh. Figure 6. shows steady-state RANS (mean) C_p comparisons with the experimental measurements, at both conditions. The plot shows an excellent match between computational and experimental values, albeit with a slight overprediction of C_p near the back end, close to the separation reattachment location.

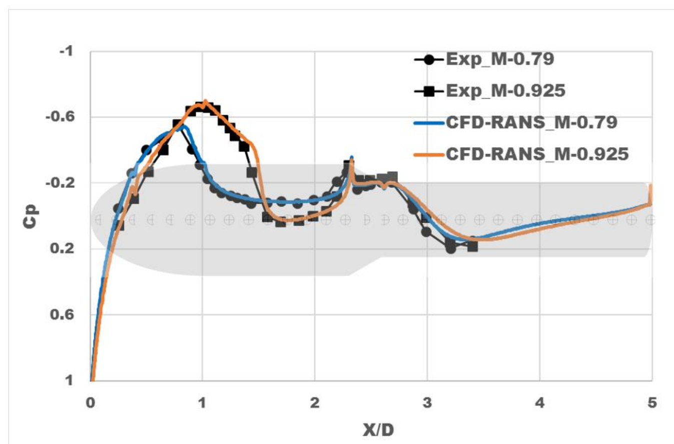

Figure 6. Model-IV, Fine Mesh Steady-State RANS (mean) Pressure Coefficient (C_p) comparisons with experimental measurements at $\alpha = 0^0$, M = 0.79 & M = 0.925

Additionally, the RANS-LES hybrid SBES model in ANSYS Fluent R19.2 was tested on Mesh 3, to predict the unsteady RMS pressure fluctuations, at first for Condition-I.

The mean and the unsteady RMS fluctuating pressure coefficients are calculated as shown in Equations 3 & 4, respectively.

$$\left(C_p\right)_{mean} = \frac{p-p_\infty}{\frac{1}{2}\rho_\infty v_\infty^2} \tag{3}$$

$$\left(\Delta C_p\right)_{RMS} = \left[\sum_n \frac{\left\{\left(C_p\right)_{mean} - \left(C_p\right)_{instantaneous}\right\}^2}{n}\right]^{\frac{1}{2}} \tag{4}$$

The scale-resolved results for Condition-I using Mesh 3 are shown in Figure 7. From this we can observe, that the RMS pressure fluctuations are not predicted accurately with an underprediction of $\left(\Delta C_p\right)_{RMS}$ near the shock location and an overprediction in the step-wake region. Similarly, Figure 8a shows the instantaneous Mach number contour overlaid by Mesh 3 near the step-wake region. The scale-resolved solution with the SBES model fails to resolve the step-wake eddies. The reason for these discrepancies is mainly due to insufficient mesh refinement in capturing turbulent fluctuations in the above defined critical regions. The unsteady SBES simulation was run with a timestep of 1.0e-5 seconds, and though convergence was achieved, a convective courant number of less than unity was reported in several parts of the mesh, including the critical regions identified above. This thus provided an indication that the mesh required further refinement in order to fully resolve the turbulent structures.

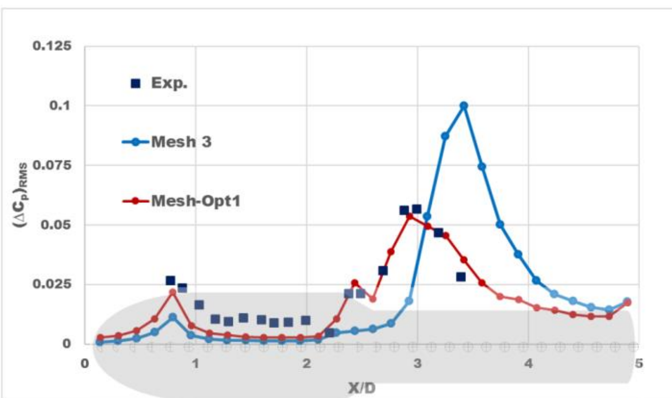

Figure 7. Model-IV, Unsteady $\left(\Delta C_p\right)_{RMS}$ pressure coefficient fluctuations, Condition-I -Mesh 3 and Mesh-Opt1.

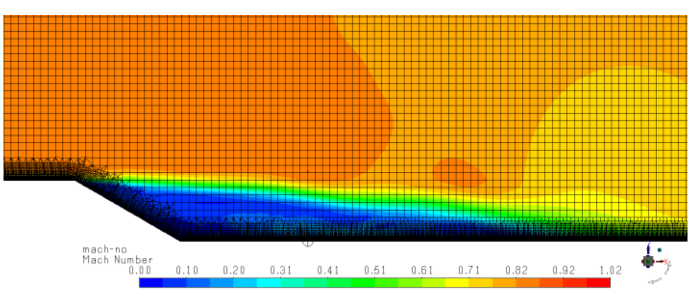

(a)

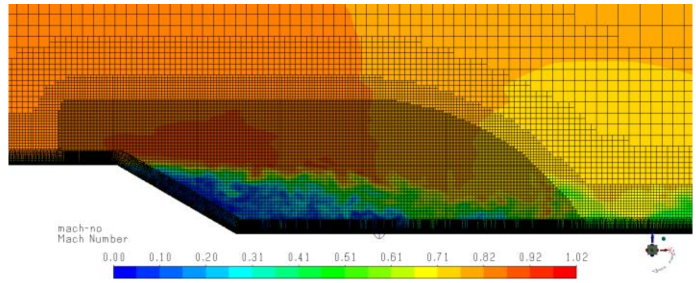

(b)

Figure 8. Model-IV, Mach contour, Condition-I, (a) Mesh 3, (b) Mesh-Opt1.

A new mesh, Mesh-Opt1, (*Figure 4)* was therefore created using local volume mesh refinement regions (done with the help of BOI definitions), identified around the body and the step-wake regions. Figure 8b shows a contour of an instantaneous Mach number overlaid with Mesh-Opt1, showing an improved capturing of the turbulent eddies, and in turn the unsteady $\left(\Delta C_p\right)_{RMS}$ pressure coefficient fluctuations *(Figure 7)*. With an improved timestep of 3.0e-6 seconds and an improved mesh, the convective courant number of unity condition was found to be satisfied and as a result, very good agreement with the experimental measurements is observed (Figure 7). The SBES simulation was run for a total flow time of 0.3 seconds. However, a small discrepancy is still observed on the middle portion of the model, after the shock and before the step. Possible reasons for this discrepancy are due to the unknown experimental uncertainties, as well as a third-party digitizer tool used to extract experimental data from the original technical report[1], dating back over 50 years. Further mesh refinement (possibly through automatic mesh adaptation) may also be needed to capture the shock more accurately.

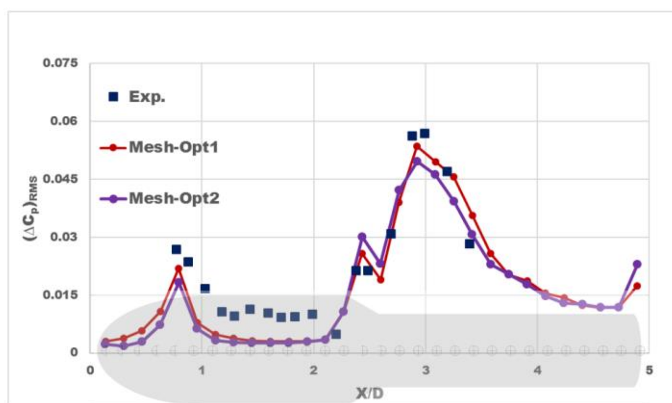

Figure 9. Model-IV, Unsteady $\left(\Delta C_p\right)_{RMS}$ pressure coefficient fluctuations, Condition-I - Mesh-Opt1 and Mesh-Opt2.

A Mosaic Poly-Hexcore mesh *(Figure 5.)* was also created using the same surface mesh and volume mesh refinement BOI specifications as those of Mesh-Opt1. Previous validations using Mosaic Poly-Hexcore mesh (Ref. 14 & 15) showed ~40% reduction in total element counts and resulted in ~14% to ~40%

faster transient SRS and steady-state RANS solutions, respectively, with similar or better solution accuracy compared to the conventional Hexcore mesh. Likewise, as seen in Figure 9, the Mosaic Poly-Hexcore mesh (Mesh-Opt2) gives predictions of the unsteady $(\Delta C_p)_{RMS}$ pressure coefficient fluctuations that are very similar to those using the conventional Hexcore mesh (Mesh-Opt1), however with a solution time that is ~35% faster and a mesh count that is ~40% less.

Figure 10 illustrates the instantaneous Mach number and pressure coefficient contours, representing the SBES solution for Condition-I on Mesh-Opt2. The Mach number contour plot indicates that the flow accelerates over the nose and reaches the upper transonic limit, with a shock seen on the front end. Flow can be observed to be separated after the 30^0 backward facing step, with reattachment observed soon after the step. A shock region can also be identified from the pressure coefficient contour *(Figure 10b)* as observed from the surface pressure jump.

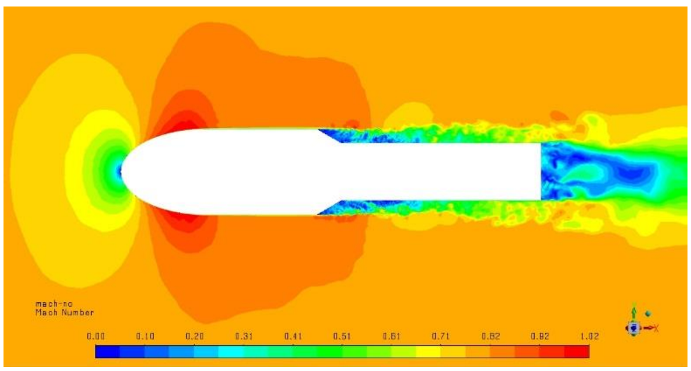

(a)

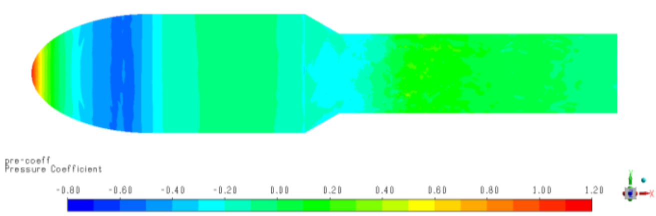

(b)

Figure 10. Model-IV, SRS, SBES, Condition-I, Mesh-Opt2 (a) Instantaneous Mach number contour, (b) Instantaneous Pressure coefficient contour.

Given the improved solution time, Condition-II ($\alpha = 0^0$ and $M = 0.925$) was then only simulated with Mesh-Opt2. Figure 11 shows the unsteady RMS pressure fluctuations compared against the experimental data.

The overall $(\Delta C_p)_{RMS}$ fluctuations generally show a good trend with the measurements, along with the correct shock location, albeit with a $(\Delta C_p)_{RMS}$ value that is noticeably lower than the reported experimental values. There is also an overprediction of $(\Delta C_p)_{RMS}$ observed close to the separation reattachment location (past the backward facing step). It is presumed that these discrepancies in critical regions are due to the need of further mesh refinement.

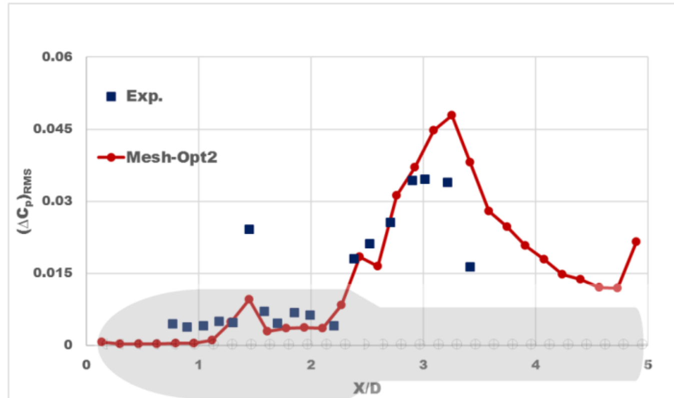

Figure 11. Model-IV, Unsteady $(\Delta C_p)_{RMS}$ pressure coefficient fluctuations, Condition-II, Mesh-Opt2.

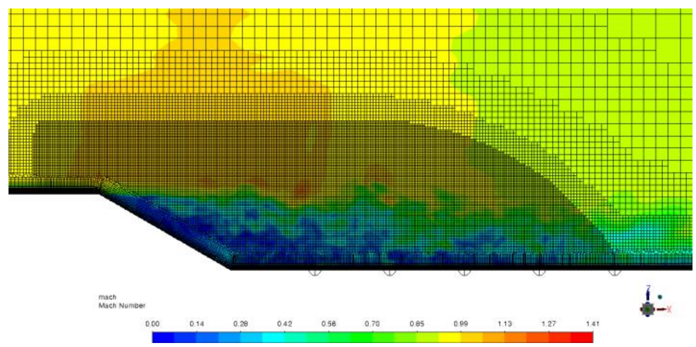

(a)

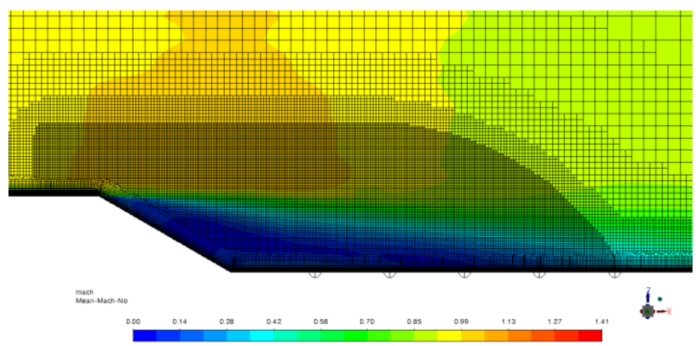

(b)

Figure 12. Model-IV, Unsteady $(\Delta C_p)_{RMS}$ pressure coefficient fluctuations, Condition-II., Mesh-Opt2. (a) Instantaneous Mach number contour, (b) Time-averaged Mach number contour.

Figure 12a and Figure 12b show the instantaneous and time-averaged Mach number contours in the step wake regions respectively. Furthermore, Figure 13a and Figure 13b show the instantaneous Mach number and pressure coefficient contour respectively. As seen from the Mach number contour the flow accelerates over the nose cone and eventually results in a stronger normal shock appearing close to X/D = 1.5. This normal shock location is accurately predicted by ANSYS Fluent R19.2 compared to the experimental mesurement, as seen from the $(\Delta C_p)_{RMS}$ plot *(Figure 11.)*. The pressure coefficient contour depicts the corresponding variation of pressure before and after the shock, respectively.

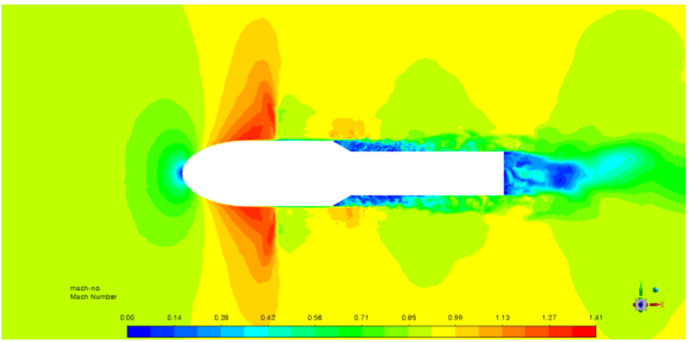

(a)

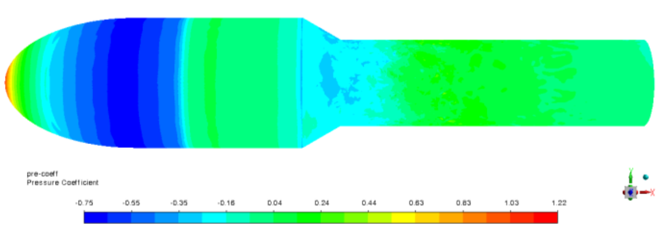

(b)

Figure 13. Model-IV, SRS, SBES, Condition-II, Mesh-Opt2 (a) Instantaneous Mach number contour, (b) Instantaneous Pressure coefficient contour.

CONCLUSIONS

The SBES model has been applied to resolve large scale turbulence essential to accurately predicting the transient fluctuations in the flow associated with a launch vehicle configuration. Beyond the application of the unsteady SBES model, the importance of a mesh that adequately spatially resolves the relevant regions of flow unsteadiness is also shown, with the insertion of appropriate mesh refinement in the step-wake region of the given model. In addition, the application of Mosaic Poly-Hexcore mesh technology was shown to significantly improve the efficieny of such computations without compromising accuracy.

The outlook is to continue these investigations for the given configuration using additional test conditions in which the angle of attack and Mach number are varied, and for which PSD measurements are available to assess the predictions of fluctuations associated with noise production. A further consideration for future work is to investigate automated mesh refinement strategies in such applications, to remove the user need for the creation of BOIs and allow for the mesh to be adapted optimally for a given set of flow conditions.

ACKNOWLEDGMENTS

The authors would like to thank Vinod Guleria from the Vikram Sarabhai Space Center (VSSC) of Indian Space Research Organization (ISRO) for his solicitation on this validation study. Also, the authors would like to thank CRAY HPC for providing computational resources for performing these simulations. Further, the authors are grateful to Laith Zori and Patrick Sharkey from ANSYS, on providing valuable inputs during the study.

Fluent Scalability on CRAY XC Series Supercomputers

The Cray XC system offers excellent parallel performance for ANSYS Fluent, with continued scaling to more than 1500 cores for ~34-million-cell Mosaic Poly-Hexcore as seen in Figure 14. Cray and ANSYS are committed to delivering high performance computing capabilities that quickly bring aerospace applications to new heights of simulation fidelity. This project is just one example of how ANSYS and Cray collaborate to build robust solutions for a broad set of engineering simulations.

Cray XC40 system combines the advantages of its Aries™ interconnect and Dragonfly network topology, Intel® Xeon® processors, integrated storage solutions, and major enhancements to the Cray Linux® Environment and programming environment. The Cray XC40 supercomputer is a ground-breaking architecture upgradable to 100 petaflops per system.

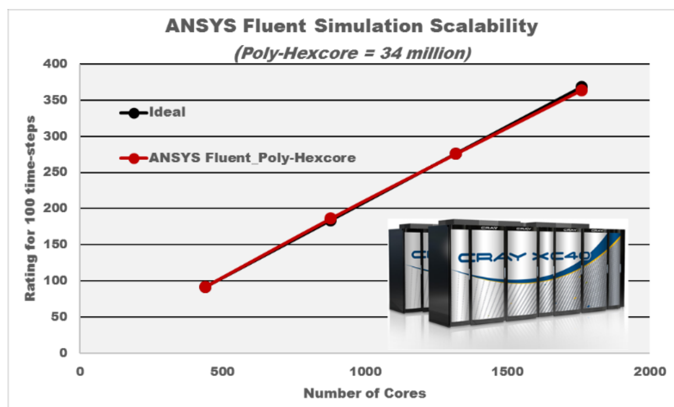

Figure 14. Fluent Scalability on CRAY XC Series Supercomputers

REFERENCES

1. Coe, Charles F.: The Effects of Some Variations in Launch-Vehicle Nose Shape on Steady and Fluctuating Pressures at Transonic Speeds. NASA TM X-646, 1962.
2. Coe, Charles F.: Steady and Fluctuating Pressures at Transonic Speeds on I Two Space-Vehicle Payload Shapes. NASA TM X-503, 1961.

3. Coe, Charles F., and Nute, James E.: Steady and Fluctuating Pressures at Transonic Speeds on Hammerhead Launch Vehicles. NASA TM X-778, 1962.
4. Gall, E. S., and Kaupp_ H._ Jr.: Fluctuating Pressure Measurements on a 32-Percent Scale Model of the Mercury Capsule_ Adapter, and Nose Portion of the Atlas Booster at Transonic Speeds. AEDC-TN-61-10, Feb. 1961.
5. Goldberg, A. P., and Wood, J. D.: Dynamic Loads in the Atlas-Able 5 During Transonic Buffeting. STL/TM-60-O000-19075, 22 Aug. 1960.
6. Goldberg_ Arthur P., and Adams_ Richard H.: Mercury-Atlas Buffeting Loads at Transonic and Low Supersonic Speeds. STL/TR-60-OOOO-AS431, 28 Nov. 1960.
7. Cleary_ Joseph W.: The Effects of Nose Bluntness on the Flow Separation and Longitudinal Characteristics of Ellipsoidal-Nosed Cylinder-Flare Models at Transonic Speeds. NASA TM X-370, 1960.
8. Emerson_ Horace F._ and Robinson_ Robert C.: The Transonic Damping in Pitch of Three Cylinder-Flare Models with Various Degrees of Nose Bluntness• NASA TM X-368, 1960.
9. Menter, F.R., "A new paradigm in hybrid RANS-LES modeling," In: Proceedings of the 6th Symposium on Hybrid RANS-LES Methods, pp. 1–17, 2016.
10. Menter, F., and Egorov, Y., 2005. “A scale adaptive simulation model using two-equation models”. AIAA (2005-1095).
11. Smagorinsky, J., (1963), “General Circulation Experiments with the Primitive Equations”, Monthly Weather Review 91, p. 99–165.
12. Nicoud, F. and Ducros, F., (1999), “Subgrid-scale stress modelling based on the square of the velocity gradient tensor”. Flow, Turb. Combust. 62, 183-200.
13. ANSYS Fluent Mosaic Technology Automatically Combines Disparate Meshes with Polyhedral Elements for Fast, Accurate Flow Resolution, https://www.ansys.com/products/fluids/ansysfluent/mosaic-meshing-technology.
14. Zore, K., Caridi, D., Lockley, I., “Fast and Accurate Prediction of Vehicle Aerodynamics using ANSYS Mosaic Mesh”. SAE COMVEC™ September 9-11, 2019, Indianapolis, IN USA. Submitted.
15. Zore, K., Parkhi, G., Sasanapuri, B., Varghese, A., “Ansys Mosaic Poly-Hexcore Mesh for High-Lift Aircraft Configuration” 21th Annual CFD Symposium, August 8-9, 2019, NAL-Bangalore India. Submitted.
16. Leonard, B., "The ULTIMATE conservative difference scheme applied to unsteady one-dimensional advection," Computer methods in applied mechanics and engineering 88(1): 17-74, 1991.